Journal of Alloys and Compounds 740 (2018) 559–566

Contents lists available at ScienceDirect

Journal of Alloys and Compounds

journal homepage: http://www.elsevier.com/locate/jalcom

Impact of Co-doping on the structural and magnetic properties of multiferroic $CaMn_7O_{12}$

A. Nonato [a], S. Yáñez-Vilar [b], M. Sánchez-Andujar [c], J. Mira [b], M.A. Señarís-Rodríguez [c], C.W.A. Paschoal [d, *]

[a] Curso Ciências Naturais, Universidade Federal do Maranhão, Campos, 65700-000, Bacabal, MA, Brazil
[b] Departamento de Física Aplicada, Universidade de Santiago de Compostela, 15782, Santiago de Compostela, Spain
[c] CICA y Departamento de Química Fundamental, Universidad de A Coruña, 15071, A Coruña, Spain
[d] Departamento de Física, Universidade Federal do Ceará, Campus do Pici, 65455-900, Fortaleza, CE, Brazil

ARTICLE INFO

Article history:
Received 23 May 2017
Received in revised form
22 November 2017
Accepted 23 November 2017
Available online 26 November 2017

Keywords:
Multiferroic
$CaMn_7O_{12}$
Quad-perovskites
Magnetoelectric
XANES

ABSTRACT

In this manuscript we showed that Co-doping into $CaMn_7O_{12}$ (CMO) induces charge disordering between Mn^{3+} and Mn^{4+} ions into the B site in the perovskite structure leading to a cubic structure $Im\bar{3}$. Both antiferromagnetic transitions at T_{N1} and T_{N2} previously observed in CMO are strongly influenced by Co-doping. The transition at T_{N1} disappears due to the structural disorder due to the Co doping, while that one at T_{N2} occurs at high temperatures. Our magnetic results explained the role of Co-doping on the magnetic ordering of CMO. Since this magnetic ordering drives the induced electric polarization in such compound, the Co doping comes up as a simple way to tune the coupling between electric polarization and magnetic helix in CMO.

© 2017 Elsevier B.V. All rights reserved.

1. Introduction

Materials with magnetically-induced polarization have been intensively investigated because of their novel physics and their potential applications in multi-functional devices [1–5]. In these materials the electric polarization is driven by noncollinear spin magnetic ordering, as in spin-current mechanism [6], by Dzyaloshinskii-Moriya interaction [7] or exchange striction mechanism [8]. According to this model the electric polarization is generated by the interaction between two neighboring spins S_i e S_{i+1} in the form $\boldsymbol{P} \propto \boldsymbol{e_{i,i+1}} \times (\boldsymbol{S_i} \times \boldsymbol{S_{i+1}})$, where $\boldsymbol{e_{i,i+1}}$ denotes the unit vector connecting the two spins [5]. This model has been quite useful to explain the induced electric polarization in some of the transition metal oxides, such as $RMnO_3$ (R=Tb, $Tb_{1-x}Dy_x$), $Ni_3V_2O_8$, $MnWO_4$ and $CoCr_2O_4$ [9–11].

Among the magnetically-induced polarization materials, $CaMn_7O_{12}$ (CMO), which belongs to the family of quad-perovskites with general molecular formula $AA'_3(B'_3B)O_{12}$, (A'=Mn^{3+}, B'=Mn^{3+} and B=Mn^{4+}), has emerged as a singular multiferroic material exhibiting the largest induced electric polarization measured so far [12]. CMO undergoes two antiferromagnetic (AFM) transitions, one at T_{N1} = 90 K and the other at T_{N2} = 45 K [13]. Below 90 K, the magnetic structure is helical, being the magnetic helix responsible for the observed large magnetically induced electric polarization [14]. This is possible due to an unconventional incommensurate orbital ordering below 250 K, since orbital ordering stabilizes the CMO chiral magnetic structure [14,15]. Furthermore, it is well known the coupling between ferroelectric and magnetic ordering observed in CMO emerges in an environment symmetry in which the Mn^{3+} and Mn^{4+} ions are ideally ordered at the B site [14].

These assumptions were recently confirmed by density functional theory calculations [16]. The 3d orbital modulation of the B' (Mn^{3+}) sites was also recently confirmed by Cao et al. [17]. They performed first-principle calculations, based on the experimentally determined modulated crystal structure, investigating the electronic and magnetic structures of CMO. Their results indicate that in the multiferroic phase the magnetic structure of the B (Mn^{4+}) sites is an harmonically modulated via orbitally-mediated coupling with the structural modulation, and that the Dzyaloshinskii-Moriya and exchange striction mechanisms contribute equally to the polarization [17]. Similar magnetic and structural features were

* Corresponding author.
E-mail address: paschoal.william@fisica.ufc.br (C.W.A. Paschoal).

https://doi.org/10.1016/j.jallcom.2017.11.260
0925-8388/© 2017 Elsevier B.V. All rights reserved.

observed into $SrMn_7O_{12}$, $PbMn_7O_{12}$ and $CdMn_7O_{12}$ [18]. Also, ferroelastic domains were observed into CMO at room temperature compatible with the rhombohedral symmetry [19,20].

Such induced electric polarization in CMO cannot be explained by the spin–current mechanism [12,14]. Currently, a more general model is employed to explain the magnetically-induced ferroelectricity in CMO. Since the chiral magnetic structure and the macroscopic structural rotation [21] couple ferroaxially, two mechanisms contribute to the ferroelectricity: i) the exchange striction interaction, which drives the polarization magnitude; ii) the Dzyaloshinskii-Moriya (DM) interaction, which drives the polarization direction [12]. Furthermore, it has been shown that Dzyaloshinskii-Moriya and exchange striction mechanisms contribute equally to the polarization [17]. Also, Radaelli et al. through a combination of neutron diffraction and Landau theory have shown that magnetic ordering in $CaMn_7O_{12}$ is characterised by a continuous evolution from a non-chiral, non-polar SDW towards a constant-moment helix with modulated spin helicity, which is both chiral and polar [22]. Thus, the multi-*k* magnetic structure in the ground state was found to be a nearly-constant-moment helix with modulated spin helicity, which oscillates in phase with the orbital occupancies on the B′ sites via trilinear magneto-orbital coupling. Also, their phenomenological model also shows that, above $T_{N2} = 48$ K, the primary magnetic order parameter is locked into the orbital wave by an admixture of helical and collinear spin density wave structures. Finally, they believe their model is quite useful to explain the lack of a sharp dielectric anomaly at T_{N1} and the unusual temperature dependence of the electrical polarization [22]. On the other hand, by using variable-temperature x-ray thermal diffuse scattering and inelastic scattering the observation of a phonon anomaly over a broad momentum regime confirmed the microscopic mechanisms of the incommensurate modulation deriving from *q*-dependent electron-phonon coupling and also from competing interactions in CMO [23].

However, it should also be indicated that Tereda et al., on the basis of pyroelectric current and bias electric field measurement results, have very recently questioned that the electric polarization observed of quad-perovskites with M = Ca, Sr, Cd, Pb is intrinsic [24]. And they rather propose that it is generated by thermally stimulated currents (TSC) [24].

Since Mn ordering play an essential role into ferroelectricity in CMO, a simple way to tune its electric polarization is by inducing a change in the charge proportion between Mn^{4+} and Mn^{3+} ions located at octahedral sites and thus modifying the magnetic ordering. This, in principle, can be done by doping the CMO compound with a trivalent ion in the A site [25]. However, it was supposed when the A site in CMO is completely occupied by trivalent ions, CMO assumes a cubic structure which results in the lack of multiferroic properties [21,26]. Recently, Jain et al. have studied magnetic and ferroelectric properties of $CaMn_7O_{12}$, doped with small amounts of isovalent Sr at the Ca-site [27]. They observed remarkable changes in the spontaneous ferroelectric polarization as well as the magnetization M with only 2% Sr doping. Particularly, in $Ca_{0.98}Sr_{0.02}Mn_7O_{12}$, they showed that polarization double and M is reduced to less than half. Finally, their results provide a clue why $SrMn_7O_{12}$ exhibits no or weak ferroelectricity [27].

Another way to modify Mn ordering in B sites in CMO, and thus its magnetic properties, is doping the compound with a trivalent ion at the B position. But in is this case there must be a mechanism by which the compound remains electrically neutral, such as: either change in the oxidation state of other cations or loss of oxygen ions. Although in principle this possibility seems rather simple, from the chemical point of view it is a challenge to dope CMO with a trivalent ion at the B site, since such cation can occupy any of the Mn sites within the structure (A′, B′ or B).

Thus, the main aim of this paper is to investigate how Co^{3+} doping can affect the structural and magnetic properties of CMO. As we will show the Co-doping ions tends to occupy the Mn^{4+} site generating charge disorder in CMO. And since the chiral magnetic structure depends on the charge ordering between Mn^{4+} and Mn^{3+} ions, changes in the magnetic properties are induced through the disorder of these cations in CMO. The obtained results allow to understand better the relationship between magnetic ordering and charge ordering in this quadruple perovskite system.

2. Experimental details

Co-doped CMO samples ($0.00 \leq x \leq 0.30$) were synthesized by the Pechini method [28], as published elsewhere [29,30] for pure CMO. Briefly, we used $Co(NO_3)_2 \cdot H_2O$ (Aldrich, >98%), $CaCO_3$ (Panreac, >98.6%) and $Mn(NO_3)_2 \cdot H_2O$ (Aldrich, >98%) as starting reagents to obtain a resin, which was decomposed at 400 °C, forming the precursor powders. The precursor powders were grounded and then heated in air at 800 °C/60 h, 900 °C/24 h, and 950 °C/24 h, respectively, with intermediate grinding and pelletizing. The resultant powders were pressed into pellets and sintered in air at 970 °C for 60 h. The samples' crystallinity was characterized by X-ray powder diffraction (XRPD) with Cu(Kα) radiation at room temperature using a Siemens D-5000 diffractometer. The obtained XRPD data were analyzed by the Rietveld profile analysis using GSAS software [31].

X-ray photoemission spectroscopy (XPS) measurements were performed in a XPS Spectrometer K-Alpha (Thermo Scientific) Al Kα micro-focused monochromator with variable spot size. High resolution spectra were acquired using energy of 50 eV, resolution of 0.1 eV, 50 acquisitions and spot with 400 nm wide. Peak position correction was done by measuring the adsorbed carbon spectrum due to exposure to atmosphere in each sample and subsequent calibration of the main carbon peak at 284.8 eV. The mean peak deviation was 0.1 eV. Shirley's background was removed using the XPS Peak program.

X-ray Absorption spectra were collected in transmission mode at room temperature at the XAFS1 beamline of the Brazilian Synchrotron Light Laboratory (Campinas, Brazil) using ion chambers as detectors and a Si(111) double crystal monochromator for energy selection. In these measurements, the storage ring operated at an energy of 4–23 keV. The energy resolution was better than 10^{-4} ΔE/E. To carry out the measurements in the transmission mode all the polycrystalline samples were deposited in polymer membranes. Such membrane has an optimum thickness for the absorption of the transition metal ion considered. For X-ray absorption near-edge spectroscopy (XANES) analysis the spectra were improved by subtracting a smooth pre-edge function from μ(E) to get rid of any instrumental background and absorption from other edges. Then the threshold energy E_0 was identified, typically as the energy of the maximum derivative of μ(E). Each spectrum was then normalized to unit absorption at about 1000 eV above the edge, where the EXAFS oscillations were not visible any more. Extended X-ray absorption fine structure (EXAFS) analyses were processed using ATHENA software [32]. The Normalized interference function χ(k) was multiplied by a Hanning window function to reduce the ripples in the Fourier-transformed spectra in r-space. The k-range for the Fourier transform was from 3.0 to 10 $Å^{-1}$.

Magnetic properties were obtained through a Quantum Design MPMS Squid magnetometer, in which zero-field-cooled (ZFC) and field-cooled (FC) magnetic susceptibility data were obtained under a field of 1000 Oe in the temperature range from 5 up to 300 K.

3. Results and discussions

Fig. 1 shows the XRPD patterns obtained for the $CaMn_{7-x}Co_xO_{12}$ samples for x = 0.00, 0.10, 0.15, 0.20 and 0.30. Clearly, cobalt doping leads to drastic changes in the crystal structure. This effect it is better seen in Fig. 1b, which shows the detailed behavior of the main diffraction peaks at 2θ~34.5°, which correspond to the (220) plane in the cubic phase. Such changes in the diffraction patterns suggest that the Co-doped CMO compounds undergo a structural phase transition for x = 0.20. To confirm this assumption we refined the XRPD patterns using the Rietveld method [33]. Fig. 2 shows such refinements. According to the obtained results, at room temperature the samples with x < 0.20 display a distorted perovskite structure with trigonal symmetry and $R\bar{3}$ space group. Meanwhile samples with 0.20 ≤ x ≤ 0.30 have cubic symmetry, space group $Im\bar{3}$. Also, we have observed weak extra diffraction peaks that reveal the presence of small amounts of Mn_3O_4 (hausmanite). Usually, impurity traces have also been observed by other authors in CMO [34,35]. In any case, these impurities, represent minor amounts (Mn_3O_4< 3%). Since the concentrations are low, its magnetic moment does not contribute effectively to the all effective magnetic moment. Thus, we disconsidered the interference of this impurity on our magnetic measurements, as it is usually assumed by other authors [34,35]. The detailed structural parameters for pure and Co-doped CMO samples are shown in Table 1. We can observe that the cell parameters and the cell volume decrease with the increase of the cobalt content.

We have performed XPS measurements to investigate the electronic structure and oxidation states of Co and Mn ions in these Co-doped CMO samples. Fig. 3a and b shows the Co2p and Mn2p XPS spectra observed for the $CaMn_{7-x}Co_xO_{12}$ (x = 0, 0.10, 0.15 and 0.20) samples, respectively. Initially, as shown in Fig. 3a, the intensities of the Co2p peaks gradually increase when the Co doping increases (x = 0.05 up to x = 0.20). However, the spectra observed for x < 0.10 do not allow to accurately predict the Co valence. Concerning the XPS spectrum observed for x = 0.20, it reveals the presence of two non-equivalent binding energies (at 779.6 eV and 780.2 eV) for the Co ion in these Co-doped samples, which are evidenced in the asymmetric shape of the mean peak. This effect can be associated with different states of the Co valence in Co-doped CMO samples. The binding energy observed at 779.6 eV ($Co2p_{3/2}$) for Co-doped samples is quite similar to that observed for

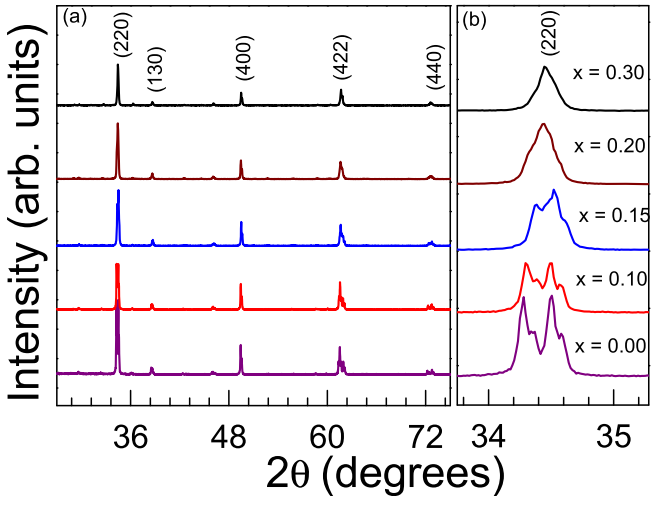

Fig. 1. (a) Room temperature XRPD patterns of $CaMn_{7-x}Co_xO_{12}$ (0.00 ≤ x ≤ 0.30). (b) Evolution of the most representative diffraction maxima with Co-doping.

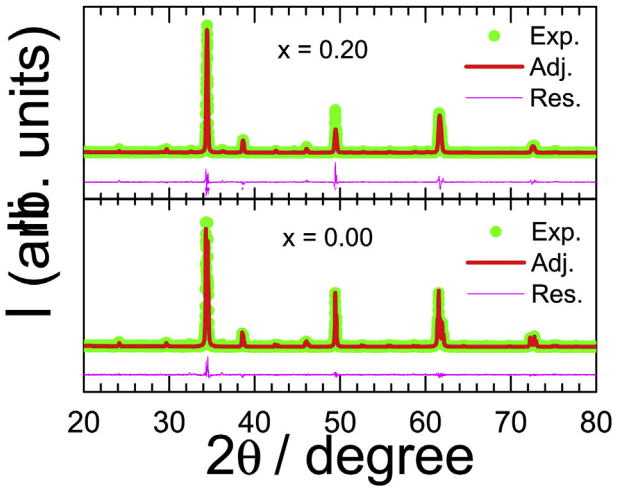

Fig. 2. Representative XRPD patterns for the (a) trigonal and (b) cubic $CaMn_{7-x}Co_xO_{12}$ samples at room temperature. The red solid line represents the curve fit obtained by the Rietveld method, while the magenta line represents the residual between the experimental data and the calculated pattern.

$La_{1-x}Sr_xCoO_3$ (779.6eV) in which Co has 3 + valence [36]. Thus, the observed binding energy at 779.6 eV is associated with Co^{3+}. In addition, the energy difference between the peak observed at 779.6 eV ($Co2p_{3/2}$) and that observed at 795.31 eV ($Co2p_{1/2}$) (not shown here) is 15.71 eV; this energy difference is characteristic of Co^{3+} [37,38]. However, we also observed another peak at about 780.2 eV ($Co2p_{3/2}$). Commonly, this binding energy is associated with Co^{2+} [39,40]. Furthermore, we observed a prominent satellite peak at about 786.4 eV, which is attributed to Co^{2+} [39]. Concerning Fig. 3b, no evident changes were observed in the Mn2p XPS spectra for the doping range considered. This suggests that the Mn valences do not change when cobalt concentration increases.

Usually, a qualitative analysis of the XPS spectrum is carried out by using the database that contains the binding energy of several transition metal oxides [41,42]. This, in principle, allows a quick analysis and often leads to a successfully determination of the valence state in the case of a simple spectrum (*i.e.* with a single peak). However, transition metal spectra may contain several features, e.g. splitting of multiplets, that cannot be appropriately addressed by making the use of these databases. So, in this work we have chosen to perform an XPS spectra analysis of the Co-doped samples considering the contributions of the multiplet components, according to Ref. [43]. Fig. 4 shows the fitted XPS spectra of Co-doped CMO samples. The fit was made by considering four peaks corresponding to Mn^{3+} components (lines in blue) and other four peaks which correspond to Mn^{4+} components (lines in orange). The fitted parameters for the pure and Co-doped CMO samples are shown in Table 2 Our results show that upon Co-doping the concentration of Mn^{4+} decreased, while the Mn^{3+} concentration exhibited the opposite trend.

Fig. 5 shows the Mn K-edge XANES spectra obtained for the $CaMn_{7-x}Co_xO_{12}$ (x = 0, 0.05, 0.10, 0.15, 0.20) samples at room temperature. The corresponding first derivatives are shown in the inset of Fig. 5. XANES spectra of reference materials for $Mn^{3+}(Mn_2O_3)$ and $Mn^{4+}(MnO_2)$ are also given. Since the XANES spectra of Co-doped samples are almost the same of the Mn3+ K-edge reference spectra, we argue that Mn valence state is predominantly 3+, and does not change with Co content increasing. On the other hand, the amplitude is slightly decreased when x = 0.20. However, this effect is expected due to Mn concentration reduction in the sample.

Table 1
Crystallographic data obtained by Rietveld refinement of the $CaMn_{7-x}Co_xO_{12}$ (CCMO) samples with $0 \leq x \leq 0.30$.

Parameter	CMO	Co-CMO(x = 0.05)	Co-CMO(x = 0.10)	Co-CMO(x = 0.15)	Co-CMO(x = 0.20)	Co-CMO(x = 0.30)
Space Group	R -3:H	R -3:H	R -3:H	R -3:H	Im-3	Im-3
a (Å)	10.4554	10.4513	10.4478	10.4388	7.3647	7.3637
b (Å)	10.4554	10.4513	10.4478	10.4388	7.3647	7.3637
c (Å)	6.3422	6.3445	6.3468	6.3519	7.3647	7.3637
V, Å3	600.78	600.53	600.29	599.79	399.45	399.29
Ca1 (x, y, z)	0, 0, 0	0, 0, 0	0, 0, 0	0, 0, 0	0, 0, 0	0, 0, 0
Mn1 (x, y, z)	0.5, 0, 0	0.5, 0, 0	0.5, 0, 0	0.5, 0, 0	0.5, 0.5, 0	0.5, 0.5, 0
Mn2 (x, y, z)	0.5, 0.5, 0.5	0.5, 0.5, 0.5	0.5, 0.5, 0.5	0.5, 0,5, 0.5	0.25, 0.25, 0.25	0.25, 0.25, 0.25
Mn3(x,y,z)	0, 0, 0.5	0, 0, 0.5	0, 0, 0.5	0, 0, 0.5	–	–
O1 x	0.2202	0.2193	0.2249	0.2063	0.2881	0.2929
y	0.2676	0.2736	0.2704	0.2493	0.1686	0.1645
z	0.0699	0.0829	0.0720	0.0805	0.0000	0.0000
O2 x	0.3389	0.3432	0.3439	0.3308	–	–
y	0.5036	0.5178	0.5181	0.5184	–	–
z	0.3596	0.3556	0.3547	0.3709	–	–
R_p (%)	11.235	12.122	15.356	12.981	16.379	16.540
wR_p (%)	14.756	18.119	20.862	19.144	24.667	25.158
Cagglioti parameters (U,V,W)	0.037, −0.018, 0.008	0.032, −0.020, 0.010	0.032, −0.018, 0.080	0.33, −0.016, 0.011	0.054, −0.046, 0.012	0.058, −0.046, 0.010
χ^2	1.334	1.281	1.376	1.491	1.994	2.142

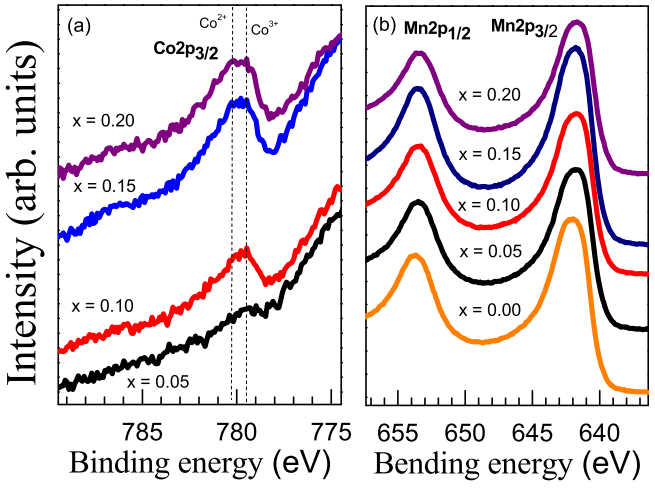

Fig. 3. XPS spectra of the $CaMn_{7-x}Co_xO_{12}$ ($0.00 \leq x \leq 0.20$): (a) Co 2p and (b) Mn 2p binding energy regions.

Fig. 6 shows the k^2-weighted Fourier transform spectra of the $CaMn_{7-x}Co_xO_{12}$ (x = 0.00, 0.10, 0.15, 0.20) at the Mn K-edges. We have observed two prominent peaks that can be associated to the first and second coordination shell, respectively. Thus, based on a two-shell model, the structural parameters obtained by nonlinear least square fits to the first two peaks of the Fourier transform spectra at the K-edges of Mn are shown in Fig. 7. As can be seen, it is clear that Mn–O, Mn–Mn and Mn–Ca bonds lengths do not significantly change with increasing Co content. This observation clearly shows that the valence of ions Mn1(Mn^{3+}), Mn2(Mn^{3+}) and Mn3(Mn^{4+}) remain unaltered since the ionic radius does not change for the doping level considered.

Thus, XPS analysis reveals that both Co^{2+} and Co^{3+} are present in these Co-doped samples. Unfortunately, we cannot estimate the proportion of these valences for the Co-doped samples. On the other hand, the Mn2p XPS analysis reveals that the Mn^{3+} concentration increases with Co concentration in the Co-doped samples, while the Mn^{4+} concentration decreases. Regarding the Mn^{3+}/Mn^{4+} proportion change we can infer two things: first, that the $Co^{3+/2+}$ ion is entering in the Mn^{4+} site and as a consequence the Mn^{3+} concentration becomes larger. Secondly, the Co-doping implies the reduction of Mn^{4+} oxidation valence ($Mn^{4+} \rightarrow Mn^{3+}$),

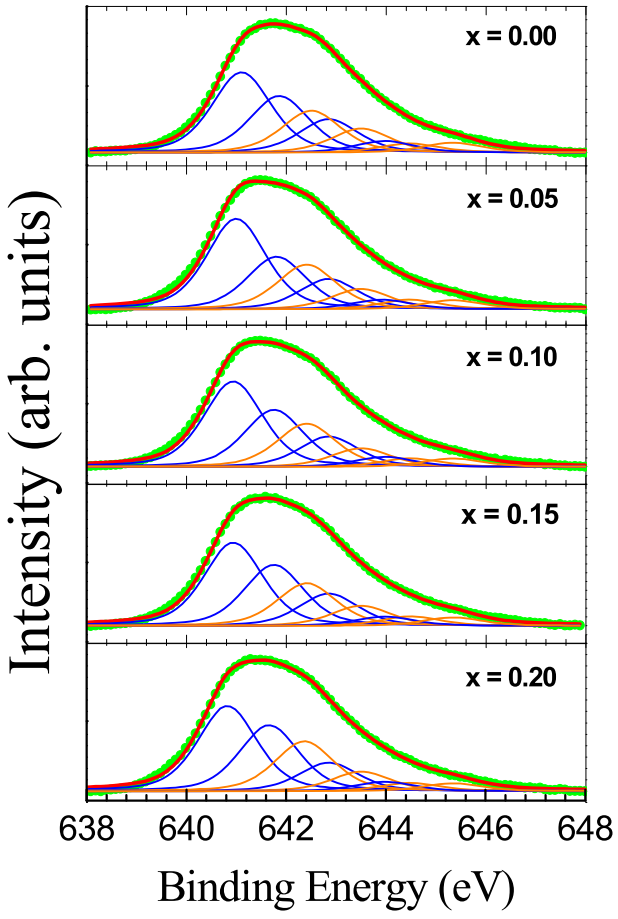

Fig. 4. Fitted XPS spectra for the $CaMn_{7-x}Co_xO_{12}$ (x = 0.00, 0.05, 0.10, 0.15 and 0.20) samples. The green bullets are the experimental data, the red line represents the curve fit, the blue line represents the Mn^{3+} multiplet component and the purple line represents the Mn^{4+} multiplet component.

and as a consequence the Mn^{3+} concentration becomes larger. This last case is quite improvable since both XPS and EXAFS analysis reveal that Mn^{3+} and Mn^{4+} do not change their valence in the indicated doping range. In this case, we propose that $Co^{2+}/^{3+}$ ions are entering in the B sites and thus replacing the Mn^{4+} ions in the

Table 2
XPS peaks obtained from the fit of the $Mn2p_{3/2}$ spectra of $CaMn_{7-x}Co_xO_{12}$ (x = 0.00, 0.05, 0.10, 0.15 and 0.20) samples. The table shows for each peak and each valence, the binding energy, in eV; its contribution to the band, in %; and its full width at half height, in eV. In addition, the total contribution for each manganese valence is given, in %, as well as the error, in %.

Sample	Valence	Peak 1			Peak 2			Peak 3			Peak 4			Total %	Error %
		Binding energy (eV)	Area (%)	FWHM (eV)	Binding energy (eV)	Area (%)	FWHM (eV)	Binding energy (eV)	Area (%)	FWHM (eV)	Binding energy (eV)	Area (%)	FWHM (eV)		
x = 0	Mn(III)	641.105	30.1	0.7	641.858	21.25	0.7	642.5	15.68	0.7	644.47	3.4	0.7	70.43	0.190
	Mn(IV)	641.858	12.52	0.7	643.5	9.02	0.7	643.97	4.32	0.7	645.335	3.68	0.7	29.54	0.094
x = 0.05	Mn(III)	640.998	34	0.7	641.804	19.72	0.7	642.405	16.74	0.7	644.47	3.59	0.7	74.05	0.210
	Mn(IV)	642.849	11.36	0.7	643.5	7.62	0.7	643.907	3.55	0.7	645.335	3.39	0.7	25.92	0.094
x = 0.10	Mn(III)	640.938	32.71	0.7	641.751	21.87	0.7	642.405	16.5	0.7	644.492	3.24	0.7	74.32	0.220
	Mn(IV)	642.849	11.58	0.7	643.5	7.08	0.7	643.97	3.81	0.7	645.335	3.18	0.7	25.65	0.086
x = 0.15	Mn(III)	640.938	31.26	0.7	641.752	22.92	0.7	642.405	16	0.7	644.492	3.56	0.7	73.74	0.200
	Mn(IV)	642.849	12.11	0.7	643.5	7.53	0.7	643.97	3.45	0.7	643.97	3.15	0.7	26.24	0.084
x = 0.20	Mn(III)	640.82	31.04	0.7	641.655	24.04	0.7	642.362	18.16	0.7	644.492	3.01	0.7	76.25	0.380
	Mn(IV)	642.849	10.36	0.7	643.5	7.1	0.7	643.97	3.42	0.7	645.335	2.87	0.7	23.75	0.120

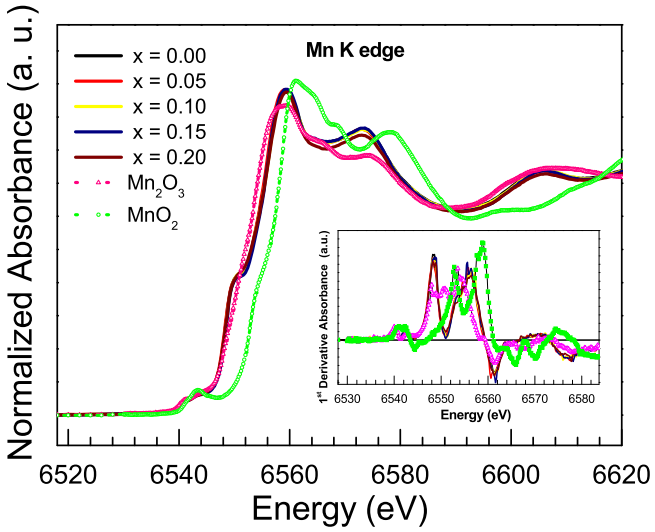

Fig. 5. Normalized XANES spectra for $CaMn_{7-x}Co_xO_{12}$ (x = 0, 0.05, 0.10, 0.15, 0.20) at the Mn K-edge compared with the Mn_2O_3 and MnO_2 spectra.

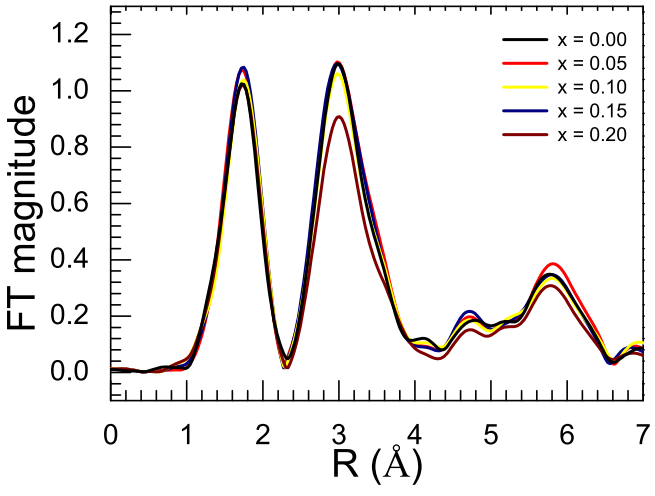

Fig. 6. k^2-weighted Fourier transform spectra of $CaMn_{7-x}Co_xO_{12}$ (x = 0.00, 0.10, 0.15, 0.20) at the Mn K-edges.

Co-doped CMO samples.

However the only possibility of this occurring is when the system displays oxygen deficiency. Thereby, we carefully investigate the chemical state of O 1s to certificate the existence of oxygen vacancies in Co-doped samples. It is well established that O 1s state contains three binding energy components, which can be described as: low binding energy peak (LP), middle binding energy peak (MP) and high binding energy peak [44]. Usually, these binding energy peaks are centred at about 530.15, 531.25 and 532.40 eV, respectively [44]. The LP is associated to O^{2-} at intrinsic sites while the MP

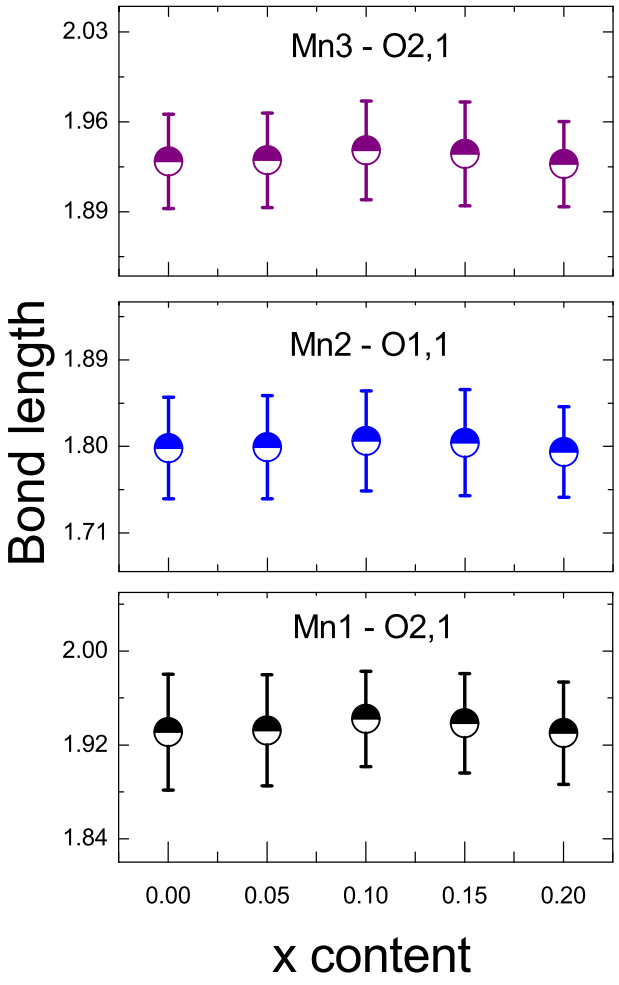

Fig. 7. Co doping dependence of first coordination shell bond lengths. Units of bond length.

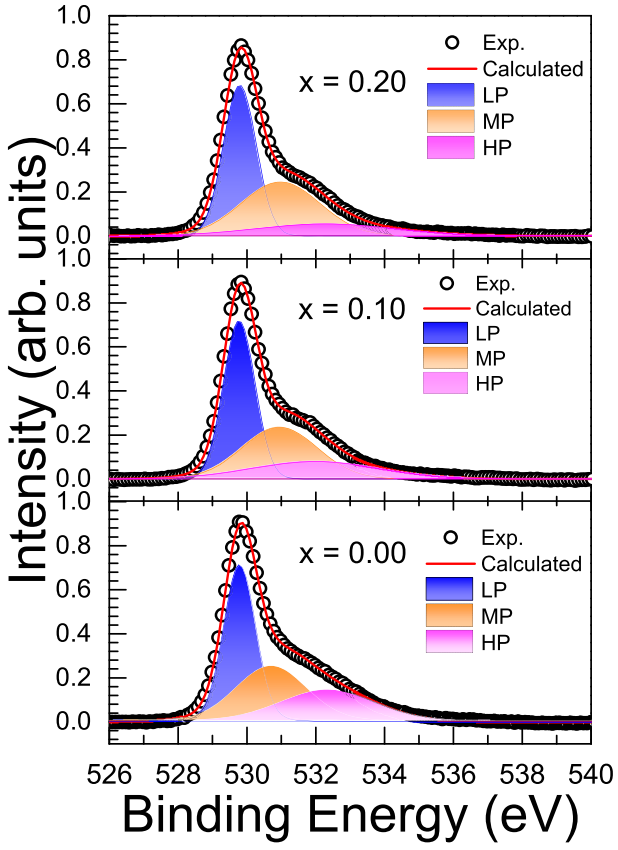

Fig. 8. XPS spectra (open circles) and simulated plots (filled area under curve) of Co-doped samples with x =0.00, 0.10 and 0.20.

is attributed to O^{2-} ions in the oxygen deficiency regions. Lastly, the HP is assigned to chemisorbed oxygen [45]. Fig. 8 shows the XPS spectra of the Co-doped samples (x = 0, 0.10 and 0.2). Using the Pseudo-Voight fitting method all the asymmetric spectra can be divided into three components (LP, MP and HP). The fitted parameters are shown in Table 3. In Fig. 8, we clearly observe that the main changes in the XPS spectra occur in the MP and HP components. As we can verify from Table 3 the area corresponding to the MP component grows whereas the area corresponding to HP component drops. This suggests that the Co-doped samples, which have a higher cobalt concentration, display greater oxygen deficiency. This is quite consistent once our results also reveal that the absorbed oxygen concentration drops for higher concentrations.

Fig. 9 shows ZFC and FC magnetic susceptibilities of Co-doped samples x = 0.00, 0.10, 0.15, and 0.20. At low temperatures the main difference between the magnetic behavior of pure and Co-doped CMO is observed around 35 K where a kind of kink can be seen in the magnetic susceptibility for the Co-doped samples. To get a detailed magnetic picture we plotted in Fig. 10 the inverse of the magnetic susceptibility as a function of temperature for all samples. From Fig. 10b we can clearly see that Co^{-}doping leads to the suppression of the first magnetic transition which occurs at T_{N1} in CMO. This transition which is characterized by a shoulder that initially emerges at 90 K (see curve for x = 0.00), slightly disappears when the Co^{-}doping increases up to x = 0.20. All the samples (x = 0.0, 0.05, 0.10, 0.15, 0.20 and 0.30) show a paramagnetic behavior above T_{N1}. In the temperature range where the magnetic susceptibility of the Co-doped samples exhibited Curie–Weiss behavior ($\chi = \frac{M}{H} = \frac{C}{T-Tc}$, in which C is the Curie constant, T is absolute temperature, and T_C is the Curie temperature), we evaluated the Curie constant and estimated the effective magnetic moment per transition metal ion (μ_{eff}/TM) through the relation $\mu_{eff} = 2.83C^{\frac{1}{2}}\mu_B$ [46]. Table 4 shows the effective magnetic moment per transition metal ion for these Co-doped samples. As it can be seen for the pure CMO (x = 0.00) μ_{eff} is almost the same observed by Sannigrahi et al. [25]. Then, upon Co-doping it increases with x up to x = 0.15 and decreases after this concentration. The small effective moment observed is usual in pure CMO and is associated to canted antiferromagnetic momentum. Similar behavior was observed by Motin Seikh et al. [47], which investigated the effects of Fe, Al and Cr doping on CMO magnetic properties.

Fig. 11 shows the reciprocal of the magnetic susceptibility derivative of the Co-doped samples as a function of temperature. As it can be seen the magnetic transition T_{N2} (lower magnetic transition) is present in all samples. However, as the Co-content increases the magnetic transition temperature T_{N2} gets higher, with the sample with x = 0.20 exhibiting this magnetic transition at around 60 K.

Our results show that Co-doped samples with x = 0.20 have cubic symmetry belonging to the space group $Im\bar{3}$.In such an structure the B site (here 8c) is occupied with a mixture of nominally Mn^{3+} and Mn^{4+} ions, which is described by an averaged ion $Mn^{3.25+}$, while the A site is occupied with Mn^{3+} ions. In addition, the average manganese in B-site forms six Mn–O equal bonds [48]. Thus, Co-doping with x ≥ 0.20 leads to a disorder in B site ions (Mn^{3+} and Mn^{4+}) in CMO. This behavior is quite similar to that observed by Motin Seikh et al., which investigated (Fe, Al, Cr)-doped CMO samples [47]. They observed that the substitution of small amounts of these trivalent cations in CMO destroys the charge ordering in the rhombohedral $R\bar{3}$ structure leading to a cubic $Im\bar{3}$ symmetry [48]. Since the magnetic transition at T_{N1} depends on the orbital ordering, and this in turn depends on the Mn^{3+}/Mn^{4+} structural ordering, the magnetic transition at T_{N1} disappear because Co concentrations higher than 2% breaks this structural ordering as observed in XRPD measurements. Therefore, as Co doping drives the structural order, this kind of doping comes out as a simple way to tune the coupling between electric polarization and magnetic helix in CMO.

4. Conclusions

The effects of Co^{-}doping on the structural and the magnetic properties of polycrystalline $CaMn_7O_{12}$ were investigated. Both structural and magnetic properties were strongly influenced by Co^{-}doping. We observed that Co-doping leads to a charge

Table 3
XPS peaks obtained from the fit of the O 1s spectra of $CaMn_{7-x}Co_xO_{12}$ (x = 0.00, 0.10 and 0.20) samples. The table shows for each peak the binding energy, in eV; its contribution to the band, in %; and its full width at half height, in eV.

Sample	Peak 1 - LP			Peak 2 - MP			Peak HP		
	Binding energy (eV)	Area (%)	FWHM (eV)	Binding energy (eV)	Area (%)	FWHM (eV)	Binding energy (eV)	Area (%)	FWHM (eV)
x = 0	529.79	43.17	1.09	530.72	32.49	2.40	532.35	24.32	3.21
x = 0.10	529.77	45.16	1.08	530.95	34.99	2.57	531.97	19.84	4.32
x = 0.20	529.79	45.67	1.12	530.97	39.08	2.68	532.27	15.24	4.71

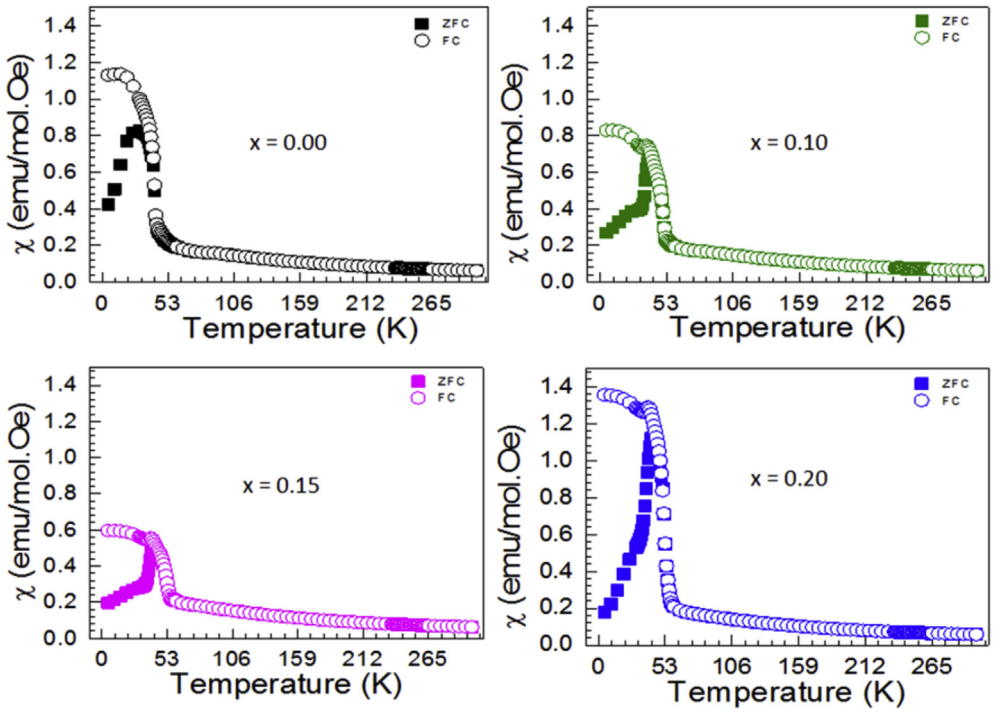

Fig. 9. Temperature-dependent FC (opened circles) and ZFC (filled squares) magnetic susceptibility of $CaMn_{7-x}Co_xO_{12}$ (0.00 < x 0.20). (a) $CaMn_7O_{12}$ and (b) $CaMn_{6.9}Co_{0.1}O_{12}$, (c) $CaMn_{6.85}Co_{0.15}O_{12}$ and (d) $CaMn_{6.8}Co_{0.2}O_{12}$ recorded under a magnetic field of 1000Oe.

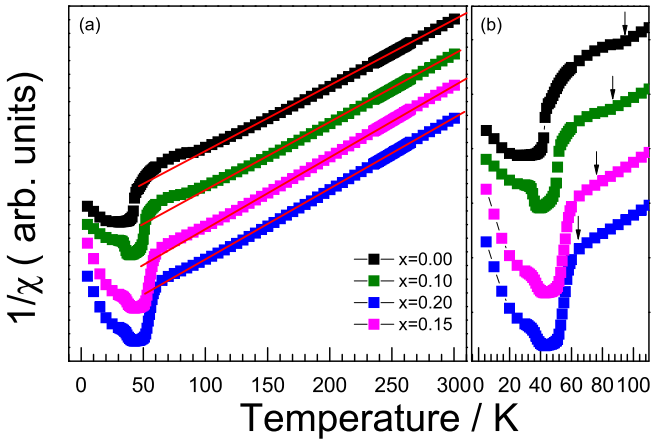

Fig. 10. (a) Temperature dependence of the inverse of the magnetic susceptibility (ZFC) of samples. (b) Zoom showing the suppression of the first magnetic transition temperature (T_{N1}).

Table 4
Effective paramagnetic moment obtained for the $CaMn_{7-x}Co_xO_{12}$ samples containing x = 0.00, 0.10, 0.15 and 0.20.

Sample	C	μ_{eff} (μ_B/Mn)
x = 0.00	133.45	4.67
x = 0.05	163.05	5.16
x = 0.10	171.02	5.29
x = 0.15	181.04	5.44
x = 0.20	120.09	4.43
x = 0.30	152.09	4.98

disordering between Mn^{4+} and Mn^{3+} at the B-site. Consequently, the compound undergoes a structural transition to a cubic phase for high Co concentrations (x ≥ 0.2). Also, the cation disordering

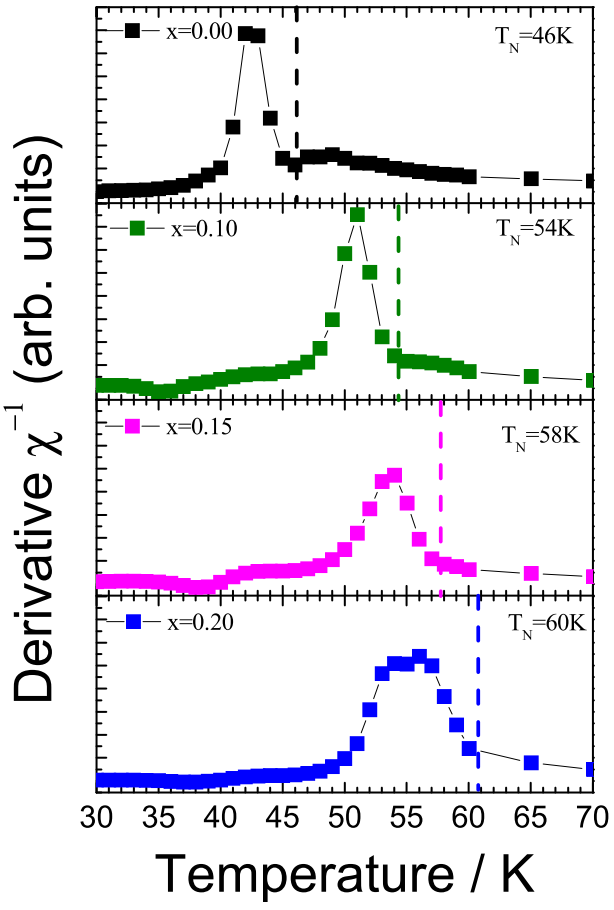

Fig. 11. Temperature-dependent of the inverse of the magnetic susceptibility (ZFC) for the $CaMn_{7-x}Co_xO_{12}$ samples containing x = 0.00, 0.10, 0.15 and 0.20.

induces changes in magnetic properties of CMO. The magnetic ordering initially observed at T_{N1} disappeared, while T_{N2} slightly increases upon cobalt doping. Our results strongly suggest that the helix magnetic is destroyed due charge disordering.

Acknowledgments

The Brazilian authors acknowledge the partial financial support from CNPq(Proc. Number 461621/2014-2), FAPEMA (Proc. Number 02121/12-PRONEM), and CAPES (Proc. Number 552512/2011-7) Brazilian funding agencies. The authors are also thanks to research supported by LNLS – Brazilian Synchrotron Light Laboratory/MCTI under research proposal number XAFS1-16869 and XAFS1-17990. The Spanish authors are grateful for the financial support from Ministerio de Economía y Competitividad MINECO and EU-FEDER under project ENE2014-56237-C4-4-R and Xunta de Galicia under project GRC2014/042, and S. Y.-V. acknowledges Xunta de Galicia for a postdoctoral grant.

References

[1] S. Dong, J.M. Liu, S.W. Cheong, Z. Ren, Multiferroic materials and magnetoelectric physics: symmetry, entanglement, excitation, and topology, Adv. Phys. 64 (2015) 519–626.
[2] M.M. Vopson, Fundamentals of multiferroic materials and their possible applications, Crit. Rev. Solid State Mater. Sci. 40 (2015) 223–250.
[3] A. Herklotz, K. Dorr, Materials science: two steps for a magnetoelectric, Nature 516 (2014) 337–338.
[4] S. Dutta, M.A. Jalaja, Ferroelectrics and multiferroics for next generation photovoltaics, Adv. Mater. Lett. 6 (2015) 568–584.
[5] M. Mostovoy, Multiferroics: a whirlwind of opportunities, Nat. Mater. 9 (2010) 188–190.
[6] H. Katsura, N. Nagaosa, A.V. Balatsky, Spin current and magnetoelectric effect in noncollinear magnets, Phys. Rev. Lett. 95 (2005), 057205.
[7] A. Sergienko, E. Dagotto, Role of the Dzyaloshinskii-Moriya interaction in multiferroic perovskites, Phys. Rev. B: Condens. Matter. Mater. Phys. 73 (2006), 094434.
[8] H. Wu, T. Burnus, Z. Hu, C. Martin, A. Maignan, J.C. Cezar, A. Tanaka, N.B. Brookes, D.I. Khomskii, L.H. Tjeng, Ising magnetism and ferroelectricity in Ca_3CoMnO_6, Phys. Rev. Lett. 102 (2009), 026404.
[9] K. Taniguchi, N. Abe, T. Takenobu, Y. Iwasa, T. Arima, Ferroelectric polarization flop in a frustrated magnet $MnWO_4$ induced by a magnetic field, Phys. Rev. Lett. 97 (2006), 097203.
[10] G. Lawes, A.B. Harris, T. Kimura, N. Rogado, R.J. Cava, A. Aharony, O. Entin-Wohlman, T. Yildirim, M. Kenzelmann, C. Broholm, A.P. Ramirez, Magnetically driven ferroelectric order in Ni_3V2O_8, Phys. Rev. Lett. 95 (2005), 087205.
[11] Y. Yamasaki, S. Miyasaka, Y. Kaneko, J.P. He, T. Arima, Y. Tokura, Magnetic reversal of the ferroelectric polarization in a multiferroic spinel oxide, Phys. Rev. Lett. 96 (2006), 207204.
[12] X.Z. Lu, M.H. Whangbo, S. Dong, X.G. Gong, H.J. Xiang, Giant ferroelectric polarization of $CaMn_7O_{12}$ induced by a combined effect of Dzyaloshinskii-Moriya interaction and exchange striction, Phys. Rev. Lett. 108 (2012), 187204.
[13] G. Zhang, S. Dong, Z. Yan, Y. Guo, S. Yunoki, E. Dagotto, J. Liu, Multiferroic properties of $CaMn_7O_{12}$, Phys. Rev. B 84 (2011), 174413.
[14] J.T. Zhang, X.M. Lu, J. Zhou, H. Sun, F.Z. Huang, J.S. Zhu, Magnetic properties and origins of ferroelectric polarization in multiferroic $CaMn_7O_{12}$, Phys. Rev. B 87 (2013), 75127.
[15] S.M. Souliou, Y. Li, X. Du, M. Le Tacon, A. Bosak, Soft-phonon-driven orbital order in $CaMn_7O_{12}$, Phys. Rev. B 94 (2016), 184309.
[16] J.Q. Dai, Y.M. Song, H. Zhang, Ferroelectric phase transition and spontaneous electric polarization in $CaMn_7O_{12}$ from first principles, New J. Phys. 17 (2015), 113038.
[17] K. Cao, R.D. Johnson, N. Perks, F. Giustino, P.G. Radaelli, First-principles study of structurally modulated multiferroic $CaMn_7O_{12}$, Phys. Rev. B: Condens. Matter Mater. Phys. 91 (2015), 064422.
[18] Y.S. Glazkova, N. Terada, Y. Matsushita, Y. Katsuya, M. Tanaka, A.V. Sobolev, I.A. Presniakov, A.A. Belik, High-pressure synthesis, crystal structures, and properties of $CdMn_7O_{12}$ and $SrMn_7O_{12}$ perovskites, Inorg. Chem. 54 (2015) 9081.
[19] R. Yuan, L. Duan, X. Du, Y. Li, Identification and mechanical control of ferroelastic domain structure in rhombohedral $CaMn_7O_{12}$, Phys. Rev. B 91 (2015), 054102.
[20] R.D. Johnson, D.D. Khalyavin, P. Manuel, P.G. Radaelli, I.S. Glazkova, N. Terada, A.A. Belik, Universal magneto-orbital ordering in the divalent A-site quadruple perovskite manganites AMn_7O_{12} (A= Ca, Sr, Cd, and Pb), Phys. Rev. B 96 (2017), 054448.
[21] N.J. Perks, R.D. Johnson, C. Martin, L.C. Chapon, P.G. Radaelli, Magneto-orbital helices as a route to coupling magnetism and ferroelectricity in multiferroic $CaMn_7O_{12}$, Nat. Commun. 3 (2012) 1277.
[22] R.D. Johnson, D.D. Khalyavin, P. Manuel, A. Bombardi, C. Martin, L.C. Chapon, P.G. Radaelli, Modulated spin helicity stabilized by incommensurate orbital density waves in a quadruple perovskite manganite, Phys. Rev. B 93 (2016), 180403.
[23] S.M. Souliou, Y. Li, X. Du, M. Le Tacon, A. Bosak, Soft-phonon-driven orbital order in $CaMn_7O_{12}$, Phys. Rev. B 94 (2016), 184309.
[24] N. Terada, Y.S. Glazkova, A.A. Belik, Differentiation between ferroelectricity and thermally stimulated current in pyrocurrent measurements of multiferroic MMn7O12 (M=Ca, Sr, Cd, Pb), Phys. Rev. B 93 (2016), 155127.
[25] J. Sannigrahi, S. Chattopadhyay, D. Dutta, S. Giri, S. Majumdar, Magnetic and electric properties of $CaMn_7O_{12}$ based multiferroic compounds: effect of electron doping, J. Phys. Condens. Matter. 25 (2013), 246001.
[26] B. Bochu, J. Chenavas, J.C. Joubert, M. Marezio, High pressure synthesis and crystal structure of a new series of perovskite-like compounds CMn_7O_{12} (C=Na, Ca, Cd, Sr, La, Nd), J. Solid State Chem. 93 (1974) 88–93.
[27] P. Jain, J. Saha, L.C. Gupta, S. Patnaik, A.K. Ganguli, R. Chatterjee, Dramatic variation of the multiferroic properties in Sr doped $Ca_{1-x}Sr_xMn_7O_{12}$, AIP Adv. 7 (2017), 055832.
[28] M.P. Pechini, Method of preparing lead and alkaline earth titanates and niobates and coating method using the same to form a capacitor, Patent 3.330.697(1967).
[29] S. Yañez-Vilar, A. Castro-Couceiro, B. Rivas-Murias, A. Fondado, J. Mira, J. Rivas, M.A. Señarís-Rodríguez, High dielectric constant in the charge-ordered manganese oxide $CaMn_7O_{12}$, Z. Anorg. Allg. Chem. 631 (2005) 2192–2196.
[30] A. Nonato, B.S. Araujo, A.P. Ayala, A.P. Maciel, Spin-phonon and magnetostriction phenomena in $CaMn_7O_{12}$ helimagnet probed by Raman spectroscopy, Appl. Phys. Lett. 105 (2014), 222902.
[31] B.H. Toby, EXPGUI, a graphical user interface for GSAS, J. Appl. Crystallogr. 34 (2001) 210–213.
[32] B. Ravel, M. Newville, ATHENA, ARTEMIS, HEPHAESTUS: data analysis for X-ray absorption spectroscopy using IFEFFIT, J. Synchrotron Rad. 12 (2005) 537–541.
[33] H.M. Rietveld, A profile refinement method for nuclear and magnetic structures, J. Appl. Crystallogr. 2 (1969) 65–71.
[34] A. Castro-Couceiro, S. Yáñez-Vilar, B. Rivas-Murias, A. Fondado, J. Mira, J. Rivas, M. Señarís-Rodríguez, Dielectric properties of the charge-ordered mixed oxide $CaMn_7O_{12}$, J. Phys. Condens. Matter. 18 (2006) 3803–3815.
[35] G. Zhang, S. Dong, Z. Yan, Y. Guo, Q. Zhang, S. Yunoki, E. Dagotto, J.M. Liu, Multiferroic properties of $CaMn_7O_{12}$, Phys. Rev. B 84 (2011), 174413.
[36] D.H. Prasad, S.Y. Park, E.O. Oh, H. Ji, H.R. Kim, K.J. Yoon, J.W. Son, J.H. Lee, Synthesis of nano-crystalline $La_{1-x}Sr_xCoO_3$ perovskite oxides by EDTA-citrate complexing process and its catalytic activity for soot oxidation, Appl. Catal. A Gen. 447–448 (2012) 100–106.
[37] N. Gunasekaran, N. Bakshi, C.B. Alcock, J.J. Carberry, Surface characterization and catalytic properties of perovskite type solid oxide solutions, $La_{0.8}Sr_{0.2}BO_3$(B=Cr, Mn, Fe, Co or Y), Solid State Ionics 83 (1996) 145–150.
[38] J. Zhang, D. Tan, Q. Meng, X. Weng, Z. Wu, Structural modification of $LaCoO_3$ perovskite for oxidation reactions: the synergistic effect of Ca^{2+} and Mg^{2+} co-substitution on phase formation and catalytic performance, Appl. Catal. B Environ. 172–173 (2015) 18–26.
[39] V. Kozhukharov, M. Machkova, P. Ivanov, H.J.M. Bouwmeester, R. Doorn, Surface analysis of doped lanthanide cobalt perovskites by X-ray photoelectron spectroscopy, J. Mater. Sci. Lett. 15 (1996) 1727–1729.
[40] M. Hassel, I. Hemmerich, H. Kuhlenbeck, H. Freund, High resolution XPS study of a thin Cr_2O_3(111) film grown on Cr(110), Surf. Sci. Spectra. 4 (1998) 246–252.
[41] J.F. Moulder, W.F. Stickle, P.E. Sobol, K.D. Bomben, Handbook of X-ray Photoelectron Spectroscopy, 1992, https://doi.org/10.1002/sia.740030412.
[42] A.V. Naumkin, A. Kraut-Vass, C.J. Powell, S. Gaarenstroom, NIST Standard Reference Database 20 Version 4.1, 2012. http://www.nist.gov/srd/.
[43] M.C. Biesinger, B.P. Payne, A.P. Grosvenor, L.W.M. Lau, A.R. Gerson, R.S.C. Smart, Resolving surface chemical states in XPS analysis of first row transition metals, oxides and hydroxides: Cr, Mn, Fe, Co and Ni, Appl. Surf. Sci. 257 (2011) 2717–2730.
[44] M. Chen, X. Wang, Y.H. Yu, Z.L. Pei, X.D. Bai, C. Sun, R.F. Huang, L.S. Wen, X-ray photoelectron spectroscopy and auger electron spectroscopy studies of Al-doped ZnO films, Appl. Surf. Sci. 158 (2000) 134–140.
[45] F. Hai-Bo, Y. Shao-Yan, Z. Pan-Feng, W. Hong-Yuan, L. Xiang-Lin, J. Chun-Mei, Z. Qin-Sheng, C. Yong-Hai, W. Zhan-Guo, Investigation of oxygen vacancy and interstitial oxygen defects in ZnO films by photoluminescence and X-Ray photoelectron spectroscopy, Chinese Phys. Lett. 24 (2007) 2108–2111.
[46] J. Yang, Y.P. Lee, Structural and magnetic properties of $Pr_{0.7}Pb_{0.3}MnO_3$, J. Korean Phys. Soc. 51 (2007) 1560–1563.
[47] M. Motin-Seikh, V. Caignaert, O.I. Lebedev, B. Raveau, Cubic structure and canted antiferromagnetism of $CaMn_7O_{12}$ doped with trivalent cations (Fe, Al, Cr), Solid State Commun. 180 (2014) 52–55.
[48] M.N. Iliev, V.G. Hadjiev, M.M. Gospodinov, R.P. Nikolova, M.V. Abrashev, Raman study of phonons in $CaMn_7O_{12}$: effects of structural modulation and structural transition, Phys. Rev. B 89 (2014), 214302.